

Learning with Explicit Shape Priors for Medical Image Segmentation

Xin You^{1,2}, Junjun He³, Jie Yang^{1,2}, and Yun Gu^{1,2}

¹ Institute of Image Processing and Pattern Recognition, Shanghai Jiao Tong University, Shanghai, China

² Institute of Medical Robotics, Shanghai Jiao Tong University, Shanghai, China

³ Shanghai AI Laboratory, Shanghai, China
{geron762, sjtu_youxin}@sjtu.edu.cn

Abstract. Medical image segmentation is considered as the basic step for medical image analysis and surgical intervention. And many previous works attempted to incorporate shape priors for designing segmentation models, which is beneficial to attain finer masks with anatomical shape information. Here in our work, we detailedly discuss three types of segmentation models with shape priors, which consist of atlas-based models, statistical-based models and UNet-based models. On the ground that the former two kinds of methods show a poor generalization ability, UNet-based models have dominated the field of medical image segmentation in recent years. However, existing UNet-based models tend to employ implicit shape priors, which do not have a good interpretability and generalization ability on different organs with distinctive shapes. Thus, we proposed a novel shape prior module (SPM), which could explicitly introduce shape priors to promote the segmentation performance of UNet-based models. To evaluate the effectiveness of SPM, we conduct experiments on three challenging public datasets. And our proposed model achieves state-of-the-art performance. Furthermore, SPM shows an outstanding generalization ability on different classic convolution-neural-networks (CNNs) and recent Transformer-based backbones, which can serve as a plug-and-play structure for the segmentation task of different datasets.

Keywords: Medical image segmentation · Explicit shape prior · UNet · BraTs 2020.

1 Introduction

Medical image segmentation is regarded as one of the most essential and challenging tasks in the filed of medical image analysis, which is beneficial to the image-guided diagnosis and surgery-based intervention [23]. Common imaging modalities contain computed tomography (CT), magnetic resonance imaging (MRI), ultrasound (US) imaging, microscopy imaging etc [44]. And medical image segmentation is aimed at providing anatomical shape information by making per-pixel predictions for organs or lesions in images [1]. Thus, many previous

works are focused on incorporating shape priors to better deal with the segmentation task. And these works can be divided into three categories, atlas-based models [27], the statistical-based gaussian mixture model (GMM) [43] and UNet-based models with specifically designed shape priors.

Atlas-based segmentation models indeed extract intensity-based transformation relations R_I between source images in atlas and target images, which is also the core step of image registration [6]. Then after applying R_I transform to source ground truths (GTs), we can attain GTs of target images. However, the registration process can be very time-consuming, and the choice of source images used for registration can be very tricky [27].

The second category of segmentation models is statistical-based models [22]. Of all statistical-based models, GMM [39] is a typical model which extracts a batch of gaussian distributions with learnable means and variances. And these distributions can serve as explicit shape priors representing shape characteristics of training datasets. Nevertheless, these models could provide a inconsistent segmentation mask as a result of imaging noise. Fixed gaussian distributions are not robust enough to cover a wide range of datasets. Thus, there may be poor segmentation results for unseen datasets [14].

In recent years, deep learning techniques [42] have dominated in various tasks of medical image analysis, image segmentation in particular. And U-shape networks [40] can extract multi-scale features for specific regions in the encoder, which contains semantic and detail information. Then deep features from the bottleneck are fused with encoded features via skip connections in the decoder structure. And deep networks are free from hand-crafted features to achieve outstanding performance for segmentation tasks.

However, current UNet-based models suffer from the following limitations. ① Segmentation masks are primarily based on the training of the final learnable prototype [57], included in the segmentation head. • Only one learnable prototype is updated per-class, thus insufficient to describe rich intra-class variance. Then it employs limited representation abilities for image segmentation tasks. • $H \times W \times D$ are mapped into $H \times W \times C$, which needs $D \times C$ parameters for prototype learning. However, this operation hurts generalization abilities [51]. ② U-shape networks do not leverage specific, anatomical or shape constraints [17]. With the perpixel cross entropy loss or dice loss, structural relations related to the regions of interest are ignored, including shapes and topology. ③ Many recent Transformer-based models are data-hungry, such as UNETR [20], Swin UNETR [45], which fail to finely learn inductive bias such as shape prior information inside data sources [53].

To solve the limitations above, prior works try to introduce anatomical shape priors to the U-shape neural networks. Clement et. [58] introduced strong shape priors from training datasets by calculating the average shape of each class offline. However, this method can only solve the segmentation for datasets with a fixed relative position. BB-UNet [16] enhanced skipped features via bounding box (BB) filters generated before training. BB filters can provide the size, shape information of the specific organ. CCBANet [37] proposed the balancing atten-

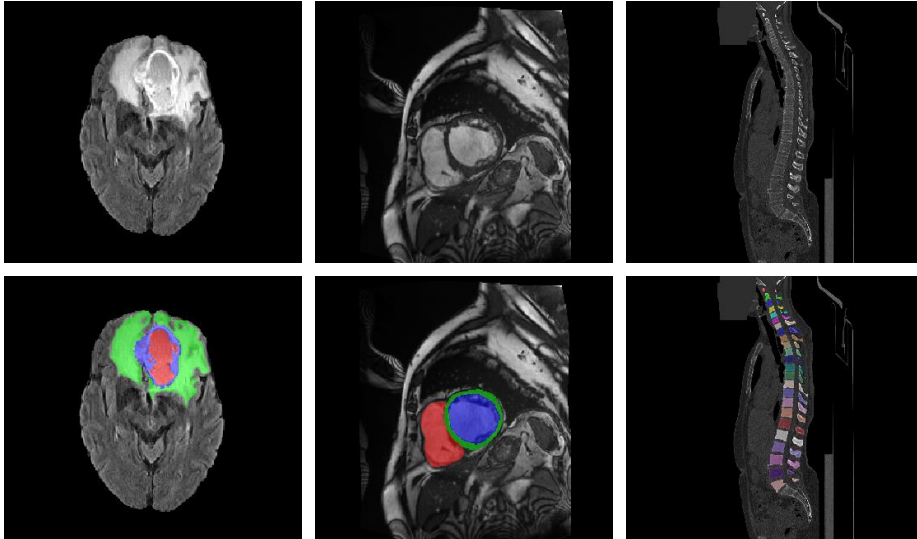


Fig. 1. Visualizations on images and ground truths of the BraTS 2020, ACDC, and VerSe 2019 datasets.

tion module (BAM) to highlight the shape context of polyps to achieve better segmentation performance. Besides, Attention UNet [38] employs attention gates (AGs) to enhance salient features beneficial for specific tasks. AGs can also suppress redundant the feature activation from irrelevant regions, which bear shape priors to some extent. CBAM [50] adopted the channel attention module and spatial attention module to boost representation abilities on the shape of specific regions. Deformable convolution [13] is proposed to introduce shape properties to convolutional kernels.

In summary, these works attempt to introduce implicit shape priors to UNet-based models, which show a weak interpretability and generalization ability on different organs with distinctive shapes. Here in our work, we intend to construct learnable explicit shape priors to promote representation powers of UNet-based models. In the field of object detection, DETR [8] introduced a set of learnable object queries, then reasons about relations of the objects and the global image context to directly output the final predictions. Motivated by this design, we devise the learnable shape prior, which is indeed a N-channel vector, and each channel contains abundant shape information for the specific class of regions. Learnable shape priors can boost encoded deep features with richer shape information, then help networks generate better masks. In the meanwhile, encoded features will contribute to iterative updates of shape priors. Based on this theory, we propose the shape prior module (SPM) to place it in the structure of skip connections. As shown in Figure 1, we evaluate SPM on three public datasets, BraTs 2020, ACDC and VerSe 2019. And we achieve the state-of-the-art segmentation performance on these datasets. Besides, due to its plug-and-play property, we probe into the generalization ability on other backbones, includ-

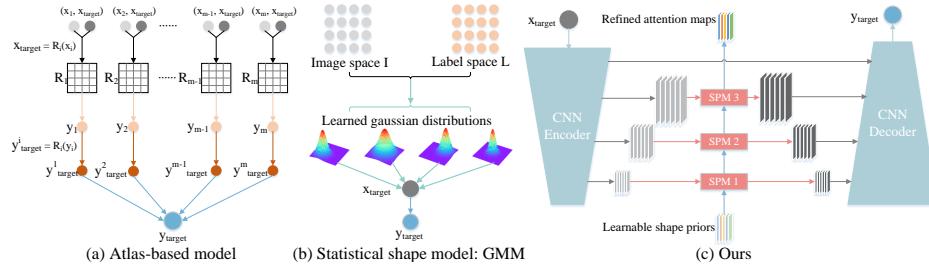


Fig. 2. The comparison between different segmentation paradigms with explicit shape priors.

ing classic convolutional-neural-networks (CNNs) and recent Transformer-based models. Experiments demonstrate that SPM can boost the segmentation performance of various models on three datasets above. Our contributions are listed as follows:

- 1) We conduct a thorough comparison analysis on three types of segmentation paradigms with explicit shape priors.
- 2) We propose a novel shape prior module (SPM), which consists of the self-update and cross-update block.
- 3) The proposed module helps us achieve SOTA performance on three public datasets, including BraTs 2020, VerSe 2019, ACDC.
- 4) SPM is a plug-and play structure, which can bring a significant boost on classic CNNs and recent Transformer backbones.

2 Methodology

2.1 Theories on Different Frameworks with explicit Shape Priors

As depicted by Figure 2, we mainly discuss about three kinds of segmentation paradigms, which can provide explicit anatomical shape priors. The first kind of paradigm is based on atlas, whose essence is the label propagation via registration relations between source and target images, from training and testing datasets [6]. Obviously, nonrigid registration cannot deal with the segmentation task due to limited data sources and imaging noise [2]. Thus, a more feasible solution is to build matching relations in a non-local way. Besides, it is beneficial to achieve a more refined segmentation mask by adopting the weighted combination of a group of candidates from source images, which are called registration bases. The segmentation masks of registration bases serve as shape priors to promote the segmentation of target images. The whole model can be described by Formula 1:

$$\mathcal{Y}_{test} = \sum_{i=1}^m \omega_i \times \mathcal{T}(\mathcal{Y}_b^i; \mathcal{R}(\mathcal{X}_b^i \Rightarrow \mathcal{X}_{test})), \mathcal{X}_b^i \in \mathcal{X}_{train}, \mathcal{Y}_b^i \in \mathcal{Y}_{train} \quad (1)$$

where \mathcal{X}_{train} and \mathcal{Y}_{train} , \mathcal{X}_{test} and \mathcal{Y}_{test} represent images and GTs from the training and testing data sources, \mathcal{X}_b and \mathcal{Y}_b represent the group of registration

bases containing m pairs of source images and GTs, ω_i is the weighting coefficient, m is the dimension of the registration space. Besides, \mathcal{R} refers to the registration transform between \mathcal{X}_b^i and \mathcal{X}_{test} . And \mathcal{T} is the transformation matrix, which applies the registration transform to each GT of registration bases \mathcal{Y}_b^i .

For atlas-based models, the choice for registration bases is significant to the robustness of segmentation performance because \mathcal{R} is indeed the projection from a single image to another image. Detailedly, the base vector should cover the distribution property of the whole dataset. If one case shows little similarity to registration bases, then we cannot gain a fine predicted mask. Furthermore, there exists a large computational cost for the inference process due to the high complexity of atlas-based models.

The second segmentation paradigm is the statistical-based models. A representative method is Gaussian Mixture Model (GMM) [39], which complete a consecutive mapping from the image space I to the label space L via a group of learnable gaussian distributions. And these gaussian distributions can be regarded as explicit shape priors from training datasets. During the training process, Expectation Maximization (EM) algorithm is iteratively implemented to update the learnable gaussian distributions and segmentation masks [43]. When dealing with the inference process for testing datasets, we utilize the learned shape priors as independent kernels. The whole model is illustrated by the following Formula:

$$\mathcal{Y}_{test} = \arg \max_{i=1, \dots, n} \mathcal{G}(\mathcal{X}_{test}; \mathcal{K}_i), \mathcal{K}_i \in \mathcal{K}(\mathcal{X}_{train}, \mathcal{Y}_{train}) \quad (2)$$

Where \mathcal{K} means learned gaussian distributions generated from the training process, \mathcal{K}_i refers to each element in \mathcal{K} , n is the number of gaussian kernels, which is also the number of semantic classes. \mathcal{G} is a mapping function by distributing n gaussian probability values to each pixel, each value generated from the kernel \mathcal{K}_i . However, GMM-based models is still sensitive to noises and dynamic backgrounds. Besides, the initial setting of the EM algorithm is crucial to the final solution, and a poor initial value tends to achieve a local optimal solution [39].

Our proposed paradigm attempts to introduce learnable explicit shape priors \mathcal{S} to U-shape neural networks. Specifically, these shape priors are utilized as inputs of UNet-based networks combined with images. And the outputs of networks are predicted masks and attention maps generated by S. Then channels of attention maps can provide abundant shape information of the ground truth region. The shape-prior-based model can be depicted as the following formula:

$$\mathcal{Y}_{test, attention} = \mathcal{F}(\mathcal{X}_{test}, \mathcal{S}(\mathcal{X}_{train}, \mathcal{Y}_{train})) \quad (3)$$

Where \mathcal{F} represents the model's forward propagation during the inference process, \mathcal{S} is a consecutive shape prior constructing the mapping between image space I and label space L . Here shape priors \mathcal{S} are updated in the training process as the image-GT pair varies. Once training finished, learnable shape priors are fixed. As shown in Figure 7, refined shape priors can be dynamically generated as

information after processed by SPM. We can have a clear visualization on features before and after being processed by SPM in Figure 9. Enhanced shape priors are made up of two components, global and local shape priors, generated from the self-update block and cross-update block respectively. We will give a more elaborate description of these two blocks.

Self-update block. On the ground that we aim to introduce explicit shape priors which can localize the target regions of interest (ROIs), the size of shape priors \mathcal{S}_o is set as $N \times$ spatial dimension. N refers to the number of classes, and spatial dimension is related to the patch size. To model the relation between inter-classes, we propose the self-update block (SUB) to generate shape priors with interactions between N channels. Motivated by the self-attention mechanism of Vision Transformer (ViT) [15], we design the self-update block. The affinity map of self-attention S_{map} between N classes is constructed by the following formula, which describes the similarity and dependency relationship between each channel of shape priors.

$$S_{map} = \text{Softmax}\left(\frac{Q_s(\mathcal{S}_o) \times K_s(\mathcal{S}_o)^T}{\sqrt{N}}\right) \quad (4)$$

Where Softmax [15] means the normalization operator, Q_s and K_s represent convolutional transforms which project \mathcal{S}_o into the query and key vector, T is the transpose operator, and the dimension for S_{map} is $N \times N$. The vanilla self-attention module shows quadratic computational complexity, which poses an obstacle to dense prediction tasks. Thus, many related works [48, 9] attempt to reduce computational costs of the self-attention module for a faster convergence and less CUDA volume. Here we set the spatial dimension of \mathcal{S}_o as $h \times w \times l$, $\frac{1}{16}$ ratio of the patch size $H \times W \times L$. Besides, \mathcal{S}_o bears N tokens, which means the self-attention module in SUB is a linear attention module. And Formula 4 shows $\mathcal{O}(N^2 \times HWL)$ computational complexity.

After that, we carry out the weighted sum of S_{map} and value vector of \mathcal{S}_o , noted as $V_s(\mathcal{S}_o)$ to calculate global shape priors. This process also requires $\mathcal{O}(N^2 \times HWL)$ computational costs. To further model the long-range dependency inside learnable shape priors, multi-layer perceptron (MLP) and layer normalization (LN) are employed. The detailed process can be illustrated as follows:

$$\mathcal{S}' = \text{LN}(S_{map} \times V_s(\mathcal{S}_o)) + \mathcal{S}_o \quad (5)$$

$$\mathcal{S}_G = \text{LN}(\text{MLP}(\mathcal{S}')) + \mathcal{S}' \quad (6)$$

Here V_s represents convolutional transforms projecting \mathcal{S}_o into the value vector, \times means the process of matrix multiplication, \mathcal{S}_G is the final global shape priors. Detailedly, \mathcal{S}_G can build the long-term dependency inside \mathcal{S}_o , which contains global contexts of sampled input patches, including coarse shape and positional representations combined with abundant texture information for global regions. We will give a detailed visualization of \mathcal{S}_G in the section 3.3.

Cross-update block. The structure of SUB falls lack of inductive bias [53] to model local visual structures and localize objects with various scales. As

a result of that, global shape priors do not have accurate shape and contour information. Further, models have to learn intrinsic inductive bias from large amounts of data for a longer training time. To address this limitation, we propose the cross-update block (CUB). Motivated by the fact that convolutional kernels intrinsically bear the inductive bias of locality and scale invariance, CUB based on convolution injects inductive bias to SPM for local shape priors with finer shape information. Moreover, based on the fact that convolutional features from the encoder have remarkable potentials to localize discriminative regions [55], we attempt to interact original skipped features F_o from the backbone with shape priors \mathcal{S}_o as demonstrated in Figure 3.

Specifically, we calculate the similarity map between features F_o and shape priors \mathcal{S}_o . Here the dimension of F_o is $C \times \frac{H}{k} \times \frac{W}{k} \times \frac{L}{k}$ ($k = 2, 4, 8$), and C represents the channel number of features. However, F_o and \mathcal{S}_o bear different scales, which makes it difficult to fuse two elements. Thus, we firstly upsample \mathcal{S}_o to the same resolution as F_o , then integrate them based on the cross attention mechanism [8]. The detailed computational process is illustrated as Formula 7:

$$C_{map} = \text{Softmax}\left(\frac{Q_c(F_o) \times K_c(\text{Upsample}(\mathcal{S}_G))^T}{\sqrt{N}}\right) \quad (7)$$

Where C_{map} means the affinity map in the cross attention stage, Q_c and K_c represent convolutional transforms which project F_o and \mathcal{S}_o into the query and key vector. C_{map} is a $C \times N$ matrix, which evaluates the relations between C -channel feature map F_o and N -channel shape priors. The specific channel of convolutional feature map F_o correlates with specific channels of shape priors. After that, C_{map} acts on transformed global shape priors \mathcal{S}_G to refine F_o , with more accurate shape characteristics and abundant global textures.

$$F_e = C_{map} \times V_c(\text{Upsample}(\mathcal{S}_G)) + F_o \quad (8)$$

Here V_c refers to convolutional transforms projecting \mathcal{S}_o into the value vector, F_e represents enhanced skipped features. At the same time, local shape priors \mathcal{S}_L are generated from downsampled F_e , which bear the property to model local visual structures (edges or corners).

$$\mathcal{S}_L = \text{Downsample}(\text{Conv}(F_e)) \quad (9)$$

$$\mathcal{S}_e = \mathcal{S}_L + \mathcal{S}_G \quad (10)$$

In conclusion, original shape priors \mathcal{S}_o are enhanced with global and local characteristics. Global shape priors can model the inter-class relations, which bear coarse shape priors with sufficient global texture information based on the self-attention block. Local shape priors show finer shape information via the introduction of inductive based on convolution. Besides, original skipped features are further enhanced via the interaction with global shape priors, which will promote to generate features with discriminative shape representations and global contexts, finally attain more accurate predicted masks.

Table 1. Comparison with other methods. Transformer models including TransUNet, Swin-UNet, TransBTS, TransBTSV2, UNETR and Swin UNETR are trained with pretrained models. (ET: the GD-enhancing tumor, WT: the whole tumor, TC: the tumor core, Mean: the average evaluation metric of three regions.)

Method	Dice score (%)				hd_{95} (mm)			
	ET	WT	TC	Mean	ET	WT	TC	Mean
VNet [35]	61.79	84.63	79.06	77.31	50.98	13.37	13.61	25.99
Deeper VNet [35]	68.97	86.11	77.90	77.66	43.53	14.50	16.15	24.72
3D UNet [12]	77.85	90.41	83.26	83.84	17.94	4.90	5.77	9.53
Liu et al. [30]	76.37	88.23	80.12	81.57	21.39	6.68	6.49	11.52
Vu et al. [47]	77.17	90.55	82.67	83.46	27.04	4.99	8.63	13.55
Nguyen et al. [36]	78.43	89.99	84.22	84.21	24.02	5.68	9.57	13.09
ResUNet [21]	78.64	90.48	85.18	84.77	17.77	6.56	5.46	9.93
TransUNet [10]	78.42	89.46	78.37	82.08	12.85	5.97	12.84	10.55
UNETR [20]	77.85	87.02	74.70	79.86	18.20	25.07	15.56	19.61
Swin UNETR [45]	79.61	89.51	84.69	84.60	14.61	11.18	6.10	10.63
UNeXt [46]	76.49	88.70	81.37	82.19	16.61	4.98	11.50	11.04
TransBTS [49]	78.73	90.09	81.73	83.52	17.95	4.96	9.77	10.89
TransBTSV2 [28]	79.63	90.56	84.50	84.90	12.52	4.27	5.56	7.45
Ours	79.70	91.08	85.35	85.38	12.06	3.92	5.08	7.02

3 Experiment

3.1 Experiment Settings

Dataset. For a thorough comparison, we conduct experiments on three public datasets for volumetric medical segmentation: the Brain Tumor Segmentation (BraTS) 2020 challenge [34, 3, 4], the Large Scale Vertebrae Segmentation Challenge (VerSe 2019) [41, 31, 29] and the Automatic Cardiac Diagnosis Challenge (ACDC) [5].

BraTS 2020: This MRI dataset contains 369 training cases, 125 validation cases and 166 testing cases. Each case bears the same volume size $155 \times 240 \times 240$ and the same voxel space $1 \times 1 \times 1$ mm. Besides, each sample consists of four modality inputs, which are T1, T1-weighted, T2-weighted and T2-FLAIR. The segmentation ground truth contains four classes, label 0 for background, label 1 for non-enhancing tumor core (NET), label 2 for peritumoral edema (ED) and label 4 for GD-enhancing tumor (ET). And the final evaluation metrics are dice scores [35] and 95% hausdorff distance hd_{95} [25] on three regions, ET region (label 4), tumor core (TC, including label 1 and 4), the whole tumor (WT, containing label 1, 2 and 4). Furthermore, we introduce the average dice score and hd_{95} for an average evaluation on three regions of interest (ROIs).

VerSe 2019: This CT dataset is composed of 80 training cases, 40 validation cases and 40 testing cases. There are 26 segmentation classes, including label 0 for the background and label 1-25 for 25 vertebrae. Of all 25 vertebrae, label 1-7 represents cervical vertebrae, label 8-19 for thoracic vertebrae and label 20-25 for lumbar vertebrae. Different samples show different field of views (FOVs), which

Table 2. Comparison with other methods. Transformer models including TransUNet, CoTr and Swin UNETR are trained with pretrained models. (Cerv: Cervical vertebrae, Thor: Thoracic vertebrae, Lumb: Lumbar vertebrae, Mean: the average evaluation metric of all vertebrae, Median: the median evaluation metric of all vertebrae.)

Method	Dice score (%)					hd_{95} (mm)				
	Cerv	Thor	Lumb	Mean	Median	Cerv	Thor	Lumb	Mean	Median
3D UNet [12]	83.10	78.37	70.88	81.28	87.54	3.26	6.27	8.50	5.80	4.02
VNet [35]	86.32	87.78	73.45	85.57	92.14	2.19	3.37	8.48	4.11	<u>1.85</u>
nnUNet [26]	87.41	88.80	74.96	<u>86.59</u>	<u>92.62</u>	2.52	3.04	7.10	4.09	2.11
TransUNet [10]	70.33	81.03	68.74	77.98	84.10	9.27	6.82	11.69	7.90	6.29
CoTr [52]	81.48	79.68	68.83	80.59	85.72	3.92	9.88	14.34	9.05	6.34
UNeXt [46]	77.00	86.73	71.06	83.36	88.39	3.44	<u>2.97</u>	9.47	4.43	2.63
maskformer [11]	76.22	80.87	72.01	83.24	89.92	2.32	7.47	9.08	6.29	2.98
EG-Trans3DUNet [54]	83.67	82.41	74.11	86.01	91.12	2.37	4.46	8.12	<u>4.03</u>	2.54
Swin UNETR [45]	<u>89.30</u>	81.43	73.36	83.46	88.91	<u>1.85</u>	5.90	8.81	5.75	3.95
Ours	89.87	<u>88.69</u>	<u>74.15</u>	87.65	93.43	1.70	2.49	<u>7.72</u>	3.58	1.78

Table 3. Comparison with other methods. Transformer models including TransUNet, Swin-UNet and UNETR are trained with pretrained models. Metric: dice scores (%). (RV: right ventricle, Myo: myocardium, LV: left ventricle, Mean: the average evaluation metric of all vertebrae.)

Method	RV	Myo	LV	Mean
R50 Att-UNet [38]	87.58	79.20	93.47	86.75
ViT-CUP [15]	81.46	70.71	92.18	81.45
R50-ViT-CUP [21]	86.07	81.88	94.75	87.57
TransUNet [10]	88.86	84.54	95.73	89.71
Swin-UNet [7]	88.55	85.62	95.83	90.00
UNETR [20]	85.29	86.52	94.02	88.61
MISSFormer [24]	86.36	85.75	91.59	87.90
LeViT-UNet-384 [19]	89.55	87.64	93.76	90.32
Maskformer [11]	87.89	87.34	94.92	90.05
nnUNet [26]	90.24	<u>89.24</u>	95.36	91.61
nnFormer [56]	<u>90.94</u>	89.58	<u>95.65</u>	<u>92.06</u>
Ours	92.28	88.13	96.61	92.34

means they may have different kinds of vertebrae. Here we select dice scores and hd_{95} for cervical, thoracic and lumbar. Besides, mean and median values for all testing cases are also reported.

ACDC: This dataset involves 100 MRI scans from 100 patients. The target ROIs are left ventricle (LV), right ventricle (RV) and myocardium (MYO). And we follow the data split setting of nnFormer [56], with 70 training cases, 10 validation cases and 20 testing cases.

Implementation Details. For the design of our proposed network as shown in Figure 2, we adopt the classic U-shape network. Specifically, we employ ResNet-50 [21] as the encoder. And the basic component of decoder is the residual block

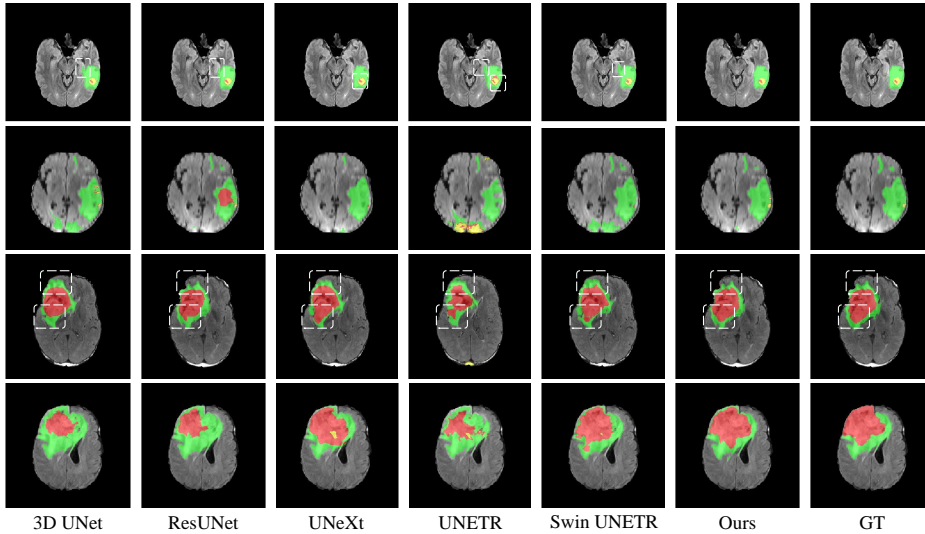


Fig. 4. Predicted segmentation masks of different models on BraTS 2020.

similar to Res-block in [45]. The proposed model is implemented in PyTorch 1.8.0 and trained on 2 NVIDIA Telsa V100, with the batch size of 2 in each GPU. All three public datasets are preprocessed with the z-score normalization [26]. For the BraTS 2020 dataset, all models are trained with the AdamW [32] optimizer for 2000 epochs, with a warm-up cosine scheduler for the first 50 epochs. The initial learning rate is set as $8e-4$ with weight decay equal to $1e-5$. And the size of cropped patches is $128 \times 128 \times 128$. We do not utilize complicated data augmentations like previous works [26, 56]. Instead, we adopt the strategies of random mirror flipping, random rotation, random intensity shift and scale. For the VerSe 2019 dataset, we train relevant models for 1000 epochs. All preprocessed cases are cropped with a patch size of $128 \times 160 \times 96$. Random rotation between $[-15^\circ, 15^\circ]$ and random flipping along the XOZ or YOZ plane are employed for the data diversity. For the ACDC dataset, models are trained for 1500 epochs and the patch size is set as $20 \times 256 \times 256$. Similarly, we augment the cardiac data with random rotation and random flipping. And for both VerSe 2019 and ACDC, we choose the Adamw optimizer with the initial learning rate set as $5e-4$ and the cosine warm-up strategy for 50 epochs during training. Following the setup in [26], we choose a sum of dice loss and cross entropy loss for model training.

3.2 Experiment Results

Brain tumor segmentation: Table 1 illustrates the quantitative segmentation performance of our proposed model compared with other CNNs and Transformer-based models. It can be figured out that our model shows the absolute superiority on the dice score and hd_{95} of all three regions. Compared with TransBTSV2 [28], our model achieves higher dice scores of 0.07%, 0.52%,

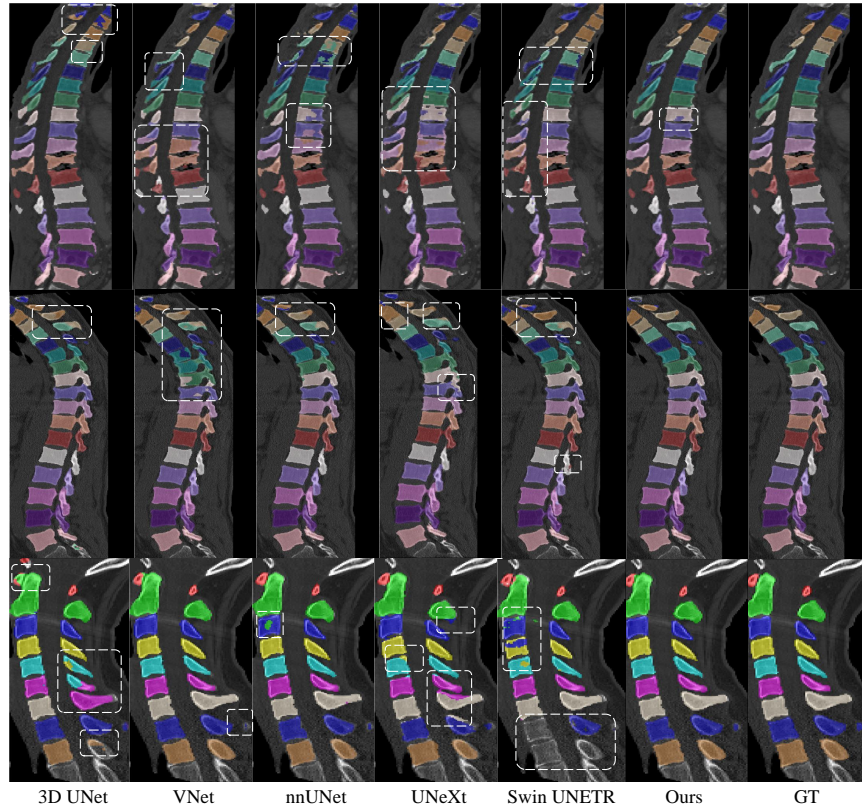


Fig. 5. Predicted segmentation masks of different models on VerSe 2019.

0.85% and a lower hd_{95} of 0.46mm, 0.35mm, 0.48mm on the ET, WT and TC region. This improvement results from the fact that enhanced shape priors serve as anatomical priors to be injected into networks, which ease the reliability on the final learnable prototype. It is worth to mention that there is a significant improvement on the metrics for Region WT and TC. We claim that our model with refined shape priors is aimed at enhance shape representations for region WT and TC, because they bear a relatively fixed shape in contrast to region ET. We will prove this viewpoint in the ablation study on the generalization abilities of SPM with different network structures.

Vertebrae segmentation: To further evaluate the performance of our proposed model, we conduct experiments on VerSe 2019. Table 2 presents the segmentation performance on the hidden test dataset. Our model outperforms the powerful nnUNet on the metric of Cervical, thoracic and the average value. Specifically, there is 2.06%, 1.06% dice score increases and 0.82mm, 0.33mm hd_{95} decreases for cervical and the whole spine. Besides, different cases have different field-of-views (FoVs), which brings difficulty for models to identify the last several vertebrae. And nnUNet is superior to other models including ours on the ability of localizing and segmenting lumbar vertebrae (Label 20-25). Furthermore, in

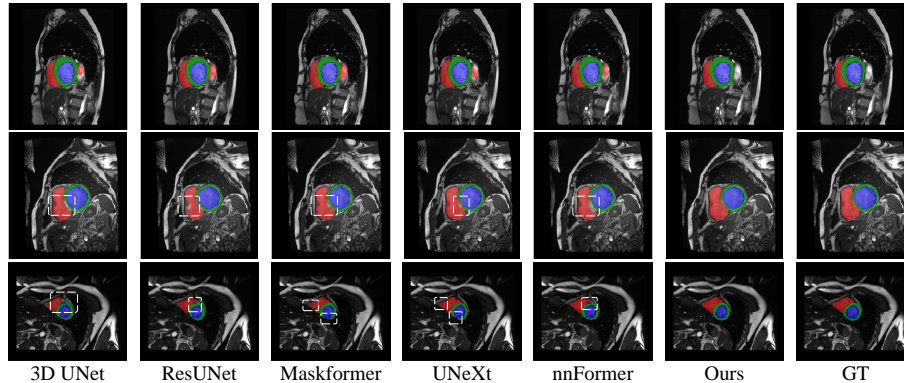


Fig. 6. Predicted segmentation masks of different models on ACDC.

contrast with other models, we achieve the highest median dice score 93.43% and 1.78mm, which means that our model can boost the overall performance of testing cases. Figure 5 illustrates that our model presents better visualization results, with more consistent predictions in a singular vertebra. This phenomenon indicates that learnable explicit shape priors for vertebrae is truly effective to the refinement of predicted masks.

Automated cardiac segmentation: We also conduct quantitative and qualitative experiments on the ACDC dataset. As shown in Table 3, our model outperforms the previous SOTA model nnFormer [56] on the evaluation metrics for the RV and LV region. Specifically, the dice scores of RV and LV reach 92.28% and 96.61%, with 1.34% and 0.96% higher than that of nnFormer. Figure 6 demonstrates that our model outputs more accurate segmentation masks, particularly in the RV and LV region. However, the segmentation performance for Myo is lower than that of nnUNet [26] and nnFormer. We argue that networks will be more focused on larger regions and ignore smaller regions due to the label imbalance between RV, LV and Myo [33]. Besides, this MRI dataset shows a large voxel space, which will aggravate the effect of label imbalance. And the unique and effective resampling strategy of nnUNet and nnFormer will improve the imbalanced distribution of the myocardium tissue, which results in stronger attentions of models on this region. Thus, nnUNet and nnFormer achieve a higher dice score on the Myo region.

3.3 Visualizations of shape priors and skipped features

In this section, we will probe into the qualitative results of shape priors and skipped features comprehensively. In fact, they are mutually enhanced. We will firstly talk about the influences of skipped features on explicit shape priors. As mentioned in section 2.1, explicit shape priors are iteratively updated under the guidance of skipped convolutional features, then optimized shape priors will activate regions of interest. We visualize two cases from the BraTS 2020 dataset in Figure 7. Case (a) illustrates generated explicit shape priors from different

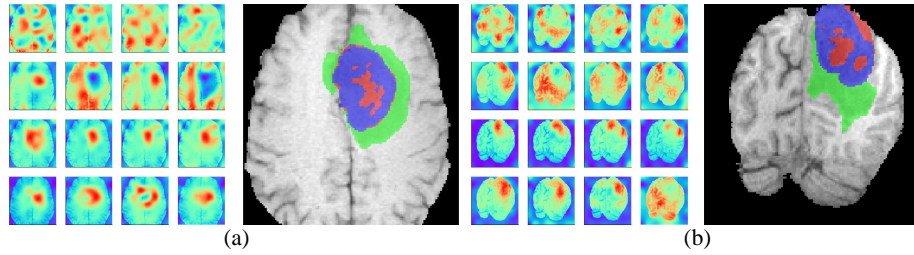


Fig. 7. Different channels (from Channel 1 to Channel 3) and different stages (from Stage 1 to Stage 3) of generated shape priors on two cases of BraTS 2020.

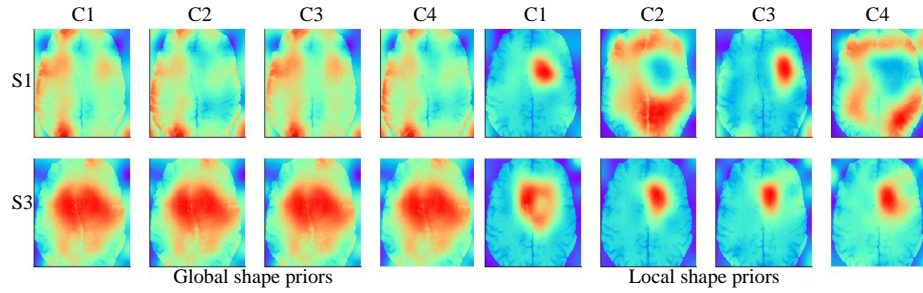


Fig. 8. Different channels and different stages of global and local shape priors on case (a) in Figure 7.

stages. Specifically, shape priors consist of N -channel attention maps, in which N refers to the number of segmentation classes, and each row represents shape priors from each stage. We can figure it out that shape priors reveal more accurate activation maps for the ground truth region as the top-to-down process. In particular, wrongly activated regions in the first stage will be suppressed in the second and third stage of SPM. Here in our visualization results, there exists a phenomenon called the reverse activation [18], which means that all regions except the ground truth area are activated. A canonical example is visualized in the last stage and last channel of shape priors in case (b). We claim that this phenomenon results from the global shape priors, which bring global contexts and abundant texture information for the whole regions, even including regions from the background. In essence, it is simple to locate the ROIs via reverse attentions, in which ROIs are highlighted with distinct contours. From this point of view, reverse activation is similar to positive activation.

Further, we decompose shape priors into two components, global and local shape priors generated from SUB and CUB respectively. We visualize these two components of case (a) in Figure 8. Due to the self-attention module [15], global shape priors bear globalized receptive fields, containing contexts and textures. However, the structure of SUB is lack in inductive bias to model local visual structures. Here we can discover that global shape priors are responsible for a coarse localization for the region of ground truths. And local shape priors

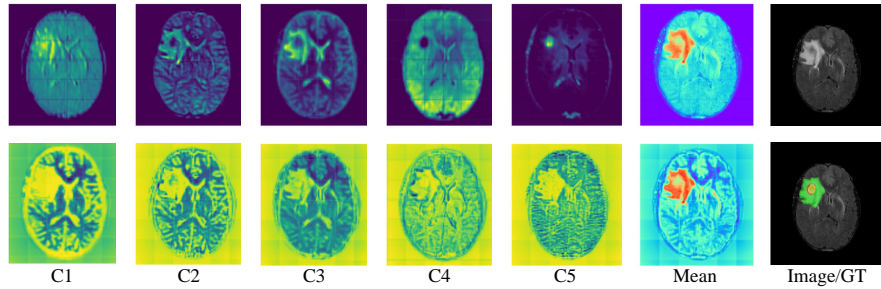


Fig. 9. Channel visualizations of skipped features before and after being processed by SPM on BraTS 2020.

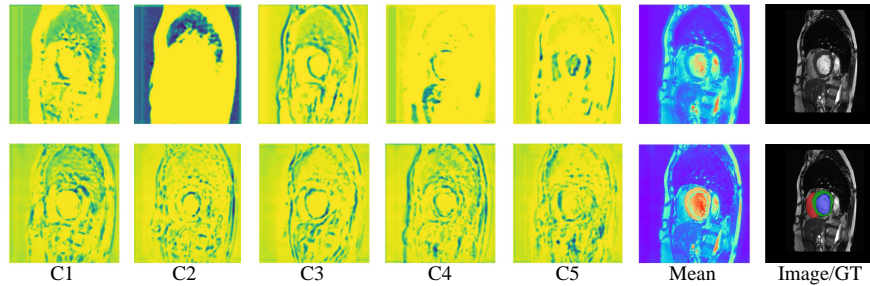


Fig. 10. Channel visualizations of skipped features before and after being processed by SPM on ACDC.

generated from CUB can provide a finer shape information for the ROIs via the introduction of convolutional kernels, which bear the inductive bias of locality.

Then we carry out a thorough analysis on the influences of shape priors on skipped features. we give a direct comparison between original skipped features F_o and enhanced skipped features F_e . In detail, We select specific channels of F_o and F_e for a qualitative visualization. As shown in Figure 9, the whole tumor region is enhanced and some voxels which are not activated before, are highlighted after being processed by SPM. Besides, via the introduction of global shape priors, skipped features are enriched with sufficient texture information for the whole region. We also explain the process of feature refinement with a cardiac CT case as shown in Figure 10. The channel-average skipped features are refined with more attentions on the LV and Myo region.

3.4 Ablation Studies

To prove the plug-and-play characteristic of SPM, we detailedly carry out ablation studies on the generalization ability of SPM on different network structures. Here we choose CNNs and Transformer-based models, including 3D UNet, ResUNet, UNETR, UNeXt and Swin UNETR. For evaluations on the BraTS 2020 dataset, we report the segmentation performance on 41 split validation cases during the training schedule. For the ACDC dataset, each MRI scan consists

Table 4. Ablation study about the generalization ability of different network structures on BraTS 2020. (ET: the GD-enhancing tumor, WT: the whole tumor, TC: the tumor core, Mean: the average evaluation metric of three regions.)

Method	Dice score (%)				hd_{95} (mm)			
	ET	WT	TC	Mean	ET	WT	TC	Mean
3D UNet [12]	82.38	91.89	90.24	88.16	4.20	4.93	3.35	4.16
+ SPM	82.86	92.42	90.46	88.58	3.77	4.26	3.28	3.77
ResUNet [21]	83.33	92.36	89.47	88.38	4.09	6.38	4.09	4.85
+ SPM	84.26	92.70	91.05	89.34	4.04	3.30	3.56	3.63
UNETR [20]	79.84	88.81	83.22	83.96	8.95	17.99	14.02	13.65
+ SPM	80.25	90.08	85.69	85.34	8.41	15.16	10.65	11.41
UNeXt [46]	79.72	91.61	89.32	86.88	4.06	4.64	4.46	4.39
+ SPM	80.61	91.89	89.75	87.42	3.40	4.11	4.39	3.97
Swin UNETR [45]	83.51	91.95	90.20	88.55	5.95	8.99	4.93	6.63
+ SPM	83.68	92.92	90.36	88.99	4.83	6.73	6.39	5.98

of thick slices, which is not applicable to the input size of UNETR and Swin UNETR. Thus, we only list out the quantitative results on 3D UNet, ResUNet and UNeXt.

According to Table 4, we have known that SPM can boost the segmentation performance of different networks. Specifically, SPM can bring an increase on ResUNet [21], with an dice score increase of 0.77%, 0.51%, 1.48% on the ET, WT, TC region. And combined with SPM, 3D UNet [12] shows an improvement on the metric of hd_{95} , with a decrease of 0.43mm, 0.67mm, 0.07mm on region ET, WT, TC. Furthermore, SPM also upgrades the segmentation performance of Transformer-based models. SPM brings an dice score increase of 1.27% and 0.97% on the WT region for UNETR [20] and Swin UNETR [45], which reveals the potential of SPM to significantly enhance the representation ability for regions with relatively regular shapes. And we can also explain this phenomenon from the perspective of inductive bias. With the introduction of shape priors, we introduce a strong inductive bias to Transformer-based models, which will relieve the requirements for a huge amount of datasets and accelerate the convergence of Transformers. Besides, SPM can improve the segmentation performance of the enhanced tumors, which bear various and irregular shapes. This phenomenon can be explained by the fact that global shape priors inject abundant global texture information to skipped features as shown in Figure 9, and these context information is effective to improve models' representation abilities for enhanced tumors.

As shown in Table 6, after employing the proposed SPM to the baseline model, there exists a significant improvement on segmentation performance of the ACDC dataset. Particularly, the dice score for the myocardium region increases by 0.98%, 2.87%, 0.57% on 3D UNet [12], ResUNet [21] and UNeXt [46] respectively. We carry out a visualization comparison between ResUNet and ResUNet with SPM. Figure 11 reveals that SPM can refine segmentation masks

Table 5. Ablation study about the generalization ability of different network structures on VerSe 2019. (Cerv: Cervical vertebrae, Thor: Thoracic vertebrae, Lumb: Lumbar vertebrae, Mean: the average evaluation metric of all vertebrae, Median: the median evaluation metric of all vertebrae.)

Method	Dice score (%)					hd_{95} (mm)				
	Cerv	Thor	Lumb	Mean	Median	Cerv	Thor	Lumb	Mean	Median
3D UNet [12]	83.10	78.37	70.88	81.28	87.54	3.26	6.27	8.50	5.80	4.02
+ SPM	85.30	84.79	72.28	84.16	90.98	2.44	5.11	9.02	5.39	3.55
ResUNet [21]	88.97	84.94	73.44	85.87	91.13	2.19	4.05	8.10	4.13	2.72
+ SPM	90.00	88.69	74.15	87.65	93.43	1.57	2.49	7.72	3.58	1.78
UNETR [20]	72.10	69.33	67.07	73.86	76.38	6.22	9.13	13.07	9.27	8.40
+ SPM	79.95	74.62	66.32	75.86	83.86	3.97	6.89	12.19	7.81	6.65
UNeXt [46]	77.00	86.73	71.06	83.36	88.39	3.44	2.97	9.47	4.43	2.63
+ SPM	85.35	86.18	73.15	84.62	91.94	2.12	3.29	7.95	4.06	1.91
Swin UNETR [45]	89.30	81.43	73.36	83.46	88.91	1.85	5.90	8.81	5.75	3.95
+ SPM	81.82	85.58	73.61	84.69	91.68	3.30	3.61	8.83	4.70	2.60

Table 6. Ablation study about the generalization ability of different network structures on ACDC. Metric: dice scores (%). (RV: right ventricle, Myo: myocardium, LV: left ventricle, Mean: the average evaluation metric of all vertebrae.)

Method	RV	Myo	LV	Mean
3D UNet [12]	91.13	85.75	95.95	90.94
+ SPM	91.78	86.73	96.29	91.60
ResUNet [21]	91.66	85.26	95.72	90.88
+ SPM	92.28	88.13	96.61	92.34
UNeXt [46]	91.85	86.91	96.34	91.70
+ SPM	92.14	87.48	96.58	92.07

with a roughly circular shape, which benefits from the learnable shape priors. Besides, false positive predictions of RV introduce inconsistency to the segmentation result of LV, which will be suppressed by anatomical shape priors learned from training datasets.

Furthermore, we conduct comprehensive experiments on VerSe 2019 to evaluate the efficacy of SPM when plugged into CNNs and Transformer-based structures. As shown in Table 5, SPM brings considerable improvements on the dice score and 95% hausdorff distance of cervical, thoracic and lumbar vertebrae. For ResUNet, the introduction of shape priors brings remarkable gains on the segmentation performance of cervical, thoracic, lumbar vertebrae, with 0.90%, 3.75%, 0.71% dice score increases and 0.49mm, 1.56mm, 0.55mm hd_{95} decreases. And for Swin UNETR [45], a Transformer-based model, substantial improvements have been achieved on the dice score and hd_{95} of thoracic vertebrae (\uparrow 4.15%, \downarrow 2.29mm). However, SPM will degrade the segmentation performance of cervical vertebrae, with the dice score decreasing by 7.48%. We argue that there are 220 cervical, 884 thoracic, 621 lumbar vertebrae in the VerSe 2019

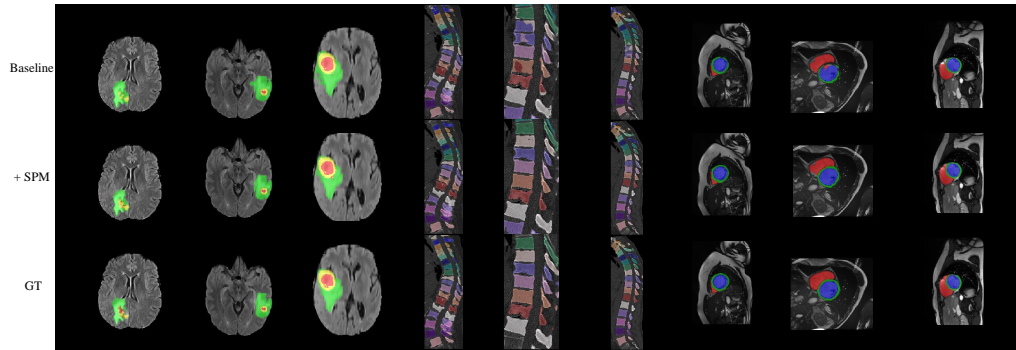


Fig. 11. Qualitative comparisons of baseline and baseline + SPM on BraTS 2020, VerSe 2019 and ACDC.

dataset [41], in which cervical vertebrae makes up a small proportion of all vertebrae. Therefore, there might be a risk of biased learning, where explicit shape priors focus on the learning of thoracic and lumbar vertebrae. Even if a segmentation degradation in the cervical region, average evaluation metrics for the whole spline is still improved, with a 1.23% dice score increase and a $1.05mm$ hd_{95} decrease. Besides, Figure 11 shows more consistent predictions in each vertebra, which is a strong proof that shape priors can enhance models’ representation abilities via the introduction of shape constraints.

4 Discussion

Quantitative and qualitative experiment results on BraTS 2020, VerSe 2019 and ACDC validate the effectiveness of SPM. Besides, as shown in Figure 7, explicit shape priors show potentials of providing sufficient shape information to guide the segmentation task. Currently, there exists a phenomenon called repetitive activation, which means that different channels of explicit shape priors tend to activate the same region. Here the affinity map S_{map} in the self-update block is employed to describe inter-relations between different channels of shape priors. And we expect to attain shape priors, in which each channel shows discriminative shape priors. Due to the fact that no constraint conditions are imposed to guide the learning of affinity map S_{map} , there still exists dependency relations between channels of global shape priors, which results in the repetitive activation in the last stage of shape priors. Furthermore, on the ground that global priors generated from SUB contains global contexts and textures for the whole region, the last-stage shape priors of some cases shows less accurate shape information than those in the second stage. As a result, the design for SUB will be a potential direction which needs to be further researched.

5 Conclusion

In this paper, we detailedly discuss three types of segmentation models with shape priors, including atlas-based models, statistical shape models and UNet-based models. To enhance the interpretability of shape priors on UNet-based models, we proposed a shape prior module (SPM), which could explicitly introduce shape priors to promote the segmentation performance on different datasets. And our model achieves state-of-the-art performance on the datasets of BraTS 2020, VerSe 2019 and ACDC. Furthermore, according to quantitative and qualitative experimental results, SPM shows a good generalization ability on different backbones, which can serve as a plug-and-play structure.

References

- [1] Reza Azad et al. “Medical image segmentation review: The success of unet”. In: *arXiv preprint arXiv:2211.14830* (2022).
- [2] M Bach Cuadra, Valérie Duay, and J-Ph Thiran. “Atlas-based segmentation”. In: *Handbook of Biomedical Imaging: Methodologies and Clinical Research* (2015), pp. 221–244.
- [3] Spyridon Bakas et al. “Advancing the cancer genome atlas glioma MRI collections with expert segmentation labels and radiomic features”. In: *Scientific data* 4.1 (2017), pp. 1–13.
- [4] Spyridon Bakas et al. “Identifying the best machine learning algorithms for brain tumor segmentation, progression assessment, and overall survival prediction in the BRATS challenge”. In: *arXiv preprint arXiv:1811.02629* (2018).
- [5] Olivier Bernard et al. “Deep learning techniques for automatic MRI cardiac multi-structures segmentation and diagnosis: is the problem solved?” In: *IEEE transactions on medical imaging* 37.11 (2018), pp. 2514–2525.
- [6] Mariano Cabezas et al. “A review of atlas-based segmentation for magnetic resonance brain images”. In: *Computer methods and programs in biomedicine* 104.3 (2011), e158–e177.
- [7] Hu Cao et al. “Swin-unet: Unet-like pure transformer for medical image segmentation”. In: *arXiv preprint arXiv:2105.05537* (2021).
- [8] Nicolas Carion et al. “End-to-end object detection with transformers”. In: *Computer Vision—ECCV 2020: 16th European Conference, Glasgow, UK, August 23–28, 2020, Proceedings, Part I 16*. Springer. 2020, pp. 213–229.
- [9] Chun-Fu Richard Chen, Quanfu Fan, and Rameswar Panda. “Crossvit: Cross-attention multi-scale vision transformer for image classification”. In: *Proceedings of the IEEE/CVF international conference on computer vision*. 2021, pp. 357–366.
- [10] Jieneng Chen et al. “Transunet: Transformers make strong encoders for medical image segmentation”. In: *arXiv preprint arXiv:2102.04306* (2021).
- [11] Bowen Cheng, Alex Schwing, and Alexander Kirillov. “Per-pixel classification is not all you need for semantic segmentation”. In: *Advances in Neural Information Processing Systems* 34 (2021), pp. 17864–17875.

- [12] Özgün Çiçek et al. “3D U-Net: learning dense volumetric segmentation from sparse annotation”. In: *International conference on medical image computing and computer-assisted intervention*. Springer. 2016, pp. 424–432.
- [13] Jifeng Dai et al. “Deformable convolutional networks”. In: *Proceedings of the IEEE international conference on computer vision*. 2017, pp. 764–773.
- [14] Aarish Shafi Dar and Devanand Padha. “Medical image segmentation: A review of recent techniques, advancements and a comprehensive comparison”. In: *Int. J. Comput. Sci. Eng* 7.7 (2019), pp. 114–124.
- [15] Alexey Dosovitskiy et al. “An Image is Worth 16x16 Words: Transformers for Image Recognition at Scale”. In: *International Conference on Learning Representations*.
- [16] Rosana El Jurdi et al. “Bb-unet: U-net with bounding box prior”. In: *IEEE Journal of Selected Topics in Signal Processing* 14.6 (2020), pp. 1189–1198.
- [17] Rosana El Jurdi et al. “High-level prior-based loss functions for medical image segmentation: A survey”. In: *Computer Vision and Image Understanding* 210 (2021), p. 103248.
- [18] Deng-Ping Fan et al. “Pranet: Parallel reverse attention network for polyp segmentation”. In: *Medical Image Computing and Computer Assisted Intervention—MICCAI 2020: 23rd International Conference, Lima, Peru, October 4–8, 2020, Proceedings, Part VI 23*. Springer. 2020, pp. 263–273.
- [19] Benjamin Graham et al. “Levit: a vision transformer in convnet’s clothing for faster inference”. In: *Proceedings of the IEEE/CVF international conference on computer vision*. 2021, pp. 12259–12269.
- [20] Ali Hatamizadeh et al. “Unetr: Transformers for 3d medical image segmentation”. In: *Proceedings of the IEEE/CVF Winter Conference on Applications of Computer Vision*. 2022, pp. 574–584.
- [21] Kaiming He et al. “Deep residual learning for image recognition”. In: *Proceedings of the IEEE conference on computer vision and pattern recognition*. 2016, pp. 770–778.
- [22] Tobias Heimann and Hans-Peter Meinzer. “Statistical shape models for 3D medical image segmentation: a review”. In: *Medical image analysis* 13.4 (2009), pp. 543–563.
- [23] Mohammad Hesam Hesamian et al. “Deep learning techniques for medical image segmentation: achievements and challenges”. In: *Journal of digital imaging* 32 (2019), pp. 582–596.
- [24] Xiaohong Huang et al. “Missformer: An effective medical image segmentation transformer”. In: *arXiv preprint arXiv:2109.07162* (2021).
- [25] Daniel P Huttenlocher, Gregory A. Klanderman, and William J Rucklidge. “Comparing images using the Hausdorff distance”. In: *IEEE Transactions on pattern analysis and machine intelligence* 15.9 (1993), pp. 850–863.
- [26] Fabian Isensee et al. “nnU-Net: a self-configuring method for deep learning-based biomedical image segmentation”. In: *Nature methods* 18.2 (2021), pp. 203–211.

- [27] Hrvoje Kalinic. “Atlas-based image segmentation: A Survey”. In: *Croatian Scientific Bibliography* (2009), pp. 1–7.
- [28] Jiangyun Li et al. “Transbtsv2: Wider instead of deeper transformer for medical image segmentation”. In: *arXiv preprint arXiv:2201.12785* (2022).
- [29] Hans Liebl et al. “A computed tomography vertebral segmentation dataset with anatomical variations and multi-vendor scanner data”. In: *Scientific Data* 8.1 (2021), p. 284.
- [30] Chenyu Liu et al. “Brain tumor segmentation network using attention-based fusion and spatial relationship constraint”. In: *Brainlesion: Glioma, Multiple Sclerosis, Stroke and Traumatic Brain Injuries: 6th International Workshop, BrainLes 2020, Held in Conjunction with MICCAI 2020, Lima, Peru, October 4, 2020, Revised Selected Papers, Part I* 6. Springer. 2021, pp. 219–229.
- [31] Maximilian T Löffler et al. “A vertebral segmentation dataset with fracture grading”. In: *Radiology: Artificial Intelligence* 2.4 (2020), e190138.
- [32] Ilya Loshchilov and Frank Hutter. “Decoupled weight decay regularization”. In: *arXiv preprint arXiv:1711.05101* (2017).
- [33] Jun Ma et al. “Loss odyssey in medical image segmentation”. In: *Medical Image Analysis* 71 (2021), p. 102035.
- [34] Bjoern H Menze et al. “The multimodal brain tumor image segmentation benchmark (BRATS)”. In: *IEEE transactions on medical imaging* 34.10 (2014), pp. 1993–2024.
- [35] Fausto Milletari, Nassir Navab, and Seyed-Ahmad Ahmadi. “V-net: Fully convolutional neural networks for volumetric medical image segmentation”. In: *2016 fourth international conference on 3D vision (3DV)*. Ieee. 2016, pp. 565–571.
- [36] Hieu T Nguyen et al. “Enhancing MRI brain tumor segmentation with an additional classification network”. In: *Brainlesion: Glioma, Multiple Sclerosis, Stroke and Traumatic Brain Injuries: 6th International Workshop, BrainLes 2020, Held in Conjunction with MICCAI 2020, Lima, Peru, October 4, 2020, Revised Selected Papers, Part I* 6. Springer. 2021, pp. 503–513.
- [37] Tan-Cong Nguyen et al. “CCBANet: cascading context and balancing attention for polyp segmentation”. In: *Medical Image Computing and Computer Assisted Intervention—MICCAI 2021: 24th International Conference, Strasbourg, France, September 27–October 1, 2021, Proceedings, Part I* 24. Springer. 2021, pp. 633–643.
- [38] Ozan Oktay et al. “Attention u-net: Learning where to look for the pancreas”. In: *arXiv preprint arXiv:1804.03999* (2018).
- [39] Douglas A Reynolds et al. “Gaussian mixture models.” In: *Encyclopedia of biometrics* 741.659-663 (2009).
- [40] Olaf Ronneberger, Philipp Fischer, and Thomas Brox. “U-net: Convolutional networks for biomedical image segmentation”. In: *International Conference on Medical image computing and computer-assisted intervention*. Springer. 2015, pp. 234–241.

- [41] Anjany Sekuboyina et al. “VerSe: A vertebrae labelling and segmentation benchmark for multi-detector CT images”. In: *Medical image analysis* 73 (2021), p. 102166.
- [42] Dinggang Shen, Guorong Wu, and Heung-Il Suk. “Deep learning in medical image analysis”. In: *Annual review of biomedical engineering* 19 (2017), pp. 221–248.
- [43] Yu-Wing Tai, Jiaya Jia, and Chi-Keung Tang. “Local color transfer via probabilistic segmentation by expectation-maximization”. In: *2005 IEEE Computer Society Conference on Computer Vision and Pattern Recognition (CVPR’05)*. Vol. 1. IEEE. 2005, pp. 747–754.
- [44] Nima Tajbakhsh et al. “Embracing imperfect datasets: A review of deep learning solutions for medical image segmentation”. In: *Medical Image Analysis* 63 (2020), p. 101693.
- [45] Yucheng Tang et al. “Self-supervised pre-training of swin transformers for 3d medical image analysis”. In: *Proceedings of the IEEE/CVF Conference on Computer Vision and Pattern Recognition*. 2022, pp. 20730–20740.
- [46] Jeya Maria Jose Valanarasu and Vishal M Patel. “Unext: Mlp-based rapid medical image segmentation network”. In: *Medical Image Computing and Computer Assisted Intervention–MICCAI 2022: 25th International Conference, Singapore, September 18–22, 2022, Proceedings, Part V*. Springer. 2022, pp. 23–33.
- [47] Minh H Vu, Tufve Nyholm, and Tommy Löfstedt. “Multi-decoder networks with multi-denoising inputs for tumor segmentation”. In: *Brainlesion: Glioma, Multiple Sclerosis, Stroke and Traumatic Brain Injuries: 6th International Workshop, BrainLes 2020, Held in Conjunction with MICCAI 2020, Lima, Peru, October 4, 2020, Revised Selected Papers, Part I* 6. Springer. 2021, pp. 412–423.
- [48] Wenhai Wang et al. “Pyramid vision transformer: A versatile backbone for dense prediction without convolutions”. In: *Proceedings of the IEEE/CVF international conference on computer vision*. 2021, pp. 568–578.
- [49] Wenxuan Wang et al. “Transbts: Multimodal brain tumor segmentation using transformer”. In: *International Conference on Medical Image Computing and Computer-Assisted Intervention*. Springer. 2021, pp. 109–119.
- [50] Sanghyun Woo et al. “Cbam: Convolutional block attention module”. In: *Proceedings of the European conference on computer vision (ECCV)*. 2018, pp. 3–19.
- [51] Zhirong Wu, Alexei A Efros, and Stella X Yu. “Improving generalization via scalable neighborhood component analysis”. In: *Proceedings of the european conference on computer vision (ECCV)*. 2018, pp. 685–701.
- [52] Yutong Xie et al. “Cotr: Efficiently bridging cnn and transformer for 3d medical image segmentation”. In: *International conference on medical image computing and computer-assisted intervention*. Springer. 2021, pp. 171–180.

- [53] Yufei Xu et al. “Vitae: Vision transformer advanced by exploring intrinsic inductive bias”. In: *Advances in Neural Information Processing Systems* 34 (2021).
- [54] Xin You et al. “EG-Trans3DUNet: a single-staged transformer-based model for accurate vertebrae segmentation from spinal CT images”. In: *2022 IEEE 19th International Symposium on Biomedical Imaging (ISBI)*. IEEE, 2022, pp. 1–5.
- [55] Bolei Zhou et al. “Learning deep features for discriminative localization”. In: *Proceedings of the IEEE conference on computer vision and pattern recognition*. 2016, pp. 2921–2929.
- [56] Hong-Yu Zhou et al. “nnFormer: Interleaved Transformer for Volumetric Segmentation”. In: *arXiv preprint arXiv:2109.03201* (2021).
- [57] Tianfei Zhou et al. “Rethinking semantic segmentation: A prototype view”. In: *Proceedings of the IEEE/CVF Conference on Computer Vision and Pattern Recognition*. 2022, pp. 2582–2593.
- [58] Clement Zotti et al. “Convolutional neural network with shape prior applied to cardiac MRI segmentation”. In: *IEEE journal of biomedical and health informatics* 23.3 (2018), pp. 1119–1128.